Journal of Asian Earth Sciences 147 (2017) 310–321

Contents lists available at ScienceDirect

Journal of Asian Earth Sciences

journal homepage: www.elsevier.com/locate/jseaes

Full length article

A gravity study along a profile across the Sichuan Basin, the Qinling Mountains and the Ordos Basin (central China): Density, isostasy and dynamics

Yongqian Zhang[a,b,*], Jiwen Teng[c], Qianshen Wang[c], Qingtian Lü[b], Xiang Si[d], Tao Xu[c,e], José Badal[f], Jiayong Yan[a,b], Zhaobing Hao[c]

[a] MLR Key Laboratory of Metallogeny and Mineral Assessment, Institute of Mineral Resources, Chinese Academy of Geological Sciences, Beijing 10037, China
[b] China Deep Exploration Center (SinoProbe Center), Chinese Academy of Geological Sciences, Beijing 100037, China
[c] State Key Laboratory of Lithosphere Evolution, Institute of Geology and Geophysics, Chinese Academy of Sciences, Beijing 100029, China
[d] Strategic Research Center of Oil & Gas Resources, Ministry of Land & Resources, Beijing 100034, China
[e] CAS Center for Excellence in Tibetan Plateau Earth Sciences, Beijing 100101, China
[f] Physics of the Earth, Sciences B, University of Zaragoza, Pedro Cerbuna 12, 50009 Zaragoza, Spain

ARTICLE INFO

Keywords:
Gravity
Density
Isostasy
Moho depth
Delamination
Middle Qinling Orogen

ABSTRACT

In order to investigate the structure of the crust beneath the Middle Qinling Mountains (MQL) and neighboring areas in the North China Block and South China Block, a north-south gravity profile from Yuquan in the Sichuan Basin to Yulin in the Ordos Basin was conducted in 2011. The Bouguer gravity anomaly is determined from a high-quality gravity dataset collected between 31°N and 36°N of latitude, and varies between −200 and −110 mGal in the study region. Using accredited velocity density relationships, an initial crust-mantle density model is constructed for MQL and adjacent areas, which is later refined interactively to simulate the observed gravity anomaly. The present study reveals the features of the density and Bouguer gravity with respect to the tectonic units sampled by the profile. The lithosphere density model shows typical density values that depict a layered structure and allow differentiate the blocks that extend along the reference profile. The gravity field calculated by forward modeling from the final density distribution model correlates well with the measured gravity field within a standard deviation of 1.26 mGal. The density in the crystalline crust increases with depth from 2.65 g/cm^3 up to the highest value of 2.95 g/cm^3 near the bottom of the crust. The Conrad interface is identified as a density jump of about 0.05 g/cm^3. The average density of the crust in MQL is clearly lower than the density in the formations on both sides. Starting from a combined Airy-Pratt isostatic compensation model, a partly compensated crust is found below MQL, suggesting future growth of the crust, unlike the Ordos and Sichuan basins that will remain stable. On the basis of the density and isostatic state of the crust and additional seismological research, such as the P-wave velocity model and Poisson's ratio, it is concluded that the lower crust delamination is a reasonable interpretation for the geophysical characteristics below the Qinling Orogen.

1. Introduction

The Qinling-Dabie Orogen crosses central China and extends about 1500 km from west to east so that it separates the North China Block to the north from the South China Block to the south (Li et al., 2007; Ratschbacher et al., 2003, 2006). This orogen contains the most abundant ultrahigh pressure metamorphic rocks in the world. On the basis of the structural features, a “three plates with two suture zones” model has been proposed and documented for this orogen (Dong et al., 2004, 2011a, 2011b, 2013; Li et al., 1996; Meng and Zhang, 1999, 2000; Zhang et al., 1995, 2001). According to this model, the Qinling Orogen was developed tectonically in the course of long multiphase processes of compression and extension, ending in a complex tectonic scenario that may well be considered as the result of the interaction between continental blocks (Fig. 1): the North China Block that includes the North Qinling Block, the South Qinling Block and the South China Block, separated from each other by the Shangdan and Mianlue sutures (Dong et al., 2004, 2011a, 2011b, 2015; Dong and Santosh, 2016; Li et al., 2007; Meng and Zhang, 1999, 2000). The Shangdan suture zone was formed by the collision between the North China Block and the South Qinling Block during the Middle Paleozoic, while the Mianlue suture zone was formed from the collision of the latter and the South

* Corresponding author at: MLR Key Laboratory of Metallogeny and Mineral Assessment, Institute of Mineral Resources, Chinese Academy of Geological Sciences, Beijing 10037, China.
E-mail address: zyq_imr@163.com (Y. Zhang).

http://dx.doi.org/10.1016/j.jseaes.2017.07.036
Received 23 December 2016; Received in revised form 17 July 2017; Accepted 19 July 2017
Available online 20 July 2017
1367-9120/

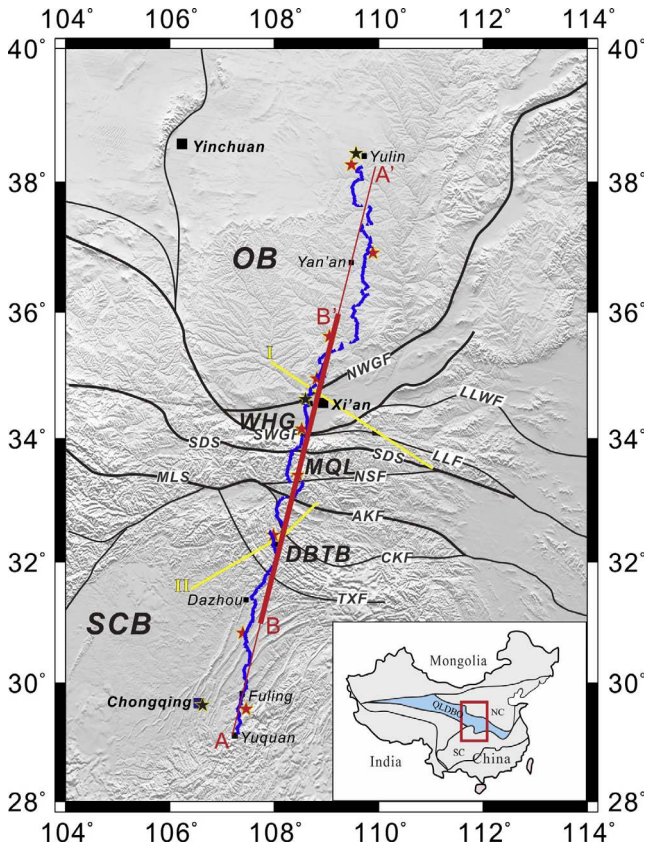

Fig. 1. Location map of the north-south integrated geophysical profile between Yuquan and Yulin (line A-A′). The inset in the bottom right corner shows the geographical position of the study area in central China. The blue triangles indicate the geographical positions of the gravity measurement points and the black stars the absolute gravity measurement points. The red stars mark the locations of the shot points fired in the course of a wide-angle seismic sounding (Teng et al., 2014a). The transect B-B′ indicates the gravity profile studied in this work. The yellow lines show two seismic profiles conducted by other authors: I, wide-angle seismic reflection/refraction profile (Ren et al., 2012); II, deep seismic reflection profile (Dong et al., 2013). Major tectonic boundaries: SDS, Shangdan suture; MLS, Mianlue suture; NWGF, North Weihe Graben fault; SWGF, South Weihe Graben fault; LLWF, Lingbao-Lushan-Wuyang fault; LLF, Luonan-Luanchuan fault; NSF, Ningshan fault; AKF, Ankang fault; CKF, Chengkou fault; TXF, Tiexi fault. Abbreviations for tectonic units are as follows: OB, Ordos Basin; WHG, Weihe Graben; MQL, Middle Qinling Mountains; DBTB, Dabashan Thrust Belt; SCB, Sichuan Basin. Abbreviations in the inset map: NC, North China Block; SC, South China Block; QLDBO, Qinling-Dabie Orogen. (For interpretation of the references to color in this figure legend, the reader is referred to the web version of this article.)

China Block during the Late Triassic.

Knowledge of the structure and history of the Qinling Orogen is important to place tight constraints on the way in which the eastern part of the Asian continent was assembled and evolved during the Phanerozoic (Mattauer et al., 1985). During the past decades, a great number of geological, geochemical and geochronological studies on the Qinling Orogen have been carried out (Ames et al., 1996; Dong et al., 2004, 2011a, 2011b, 2015; Dong and Santosh, 2016; Gao et al., 1995; Hacker et al., 1998; Li et al., 1996, 2007; Mattauer et al., 1985; Meng and Zhang, 1999, 2000; Ratschbacher et al., 2003, 2006; Wu et al., 2014; Zhang et al., 1995, 1996, 1997, 2001). Some geophysical investigations have also been performed, including teleseismic studies (He et al., 1998; Huang et al., 2014), wide-angle seismic reflection/refraction soundings (Ren et al., 2012; Teng et al., 2014a, 2014b; Zhang et al., 2008a), deep seismic reflection profiles (Dong et al., 2013; Gao et al., 2014; Li et al., 2015; Wang et al., 2007; Yuan et al., 1994) and a magneto-telluric study (Cheng et al., 2003); all of them have allowed to better understand the deep structure and characteristics of the crust and upper mantle throughout the Qinling Orogen. However, the existing geophysical research on Qinling focuses mainly on the eastern segment (He et al., 1998; Yuan et al., 1994; Zhang et al., 1996) or the western segment (Gao et al., 2014; Wang et al., 2007; Zhang et al., 2007, 2008a); only a few studies focus on the deep structure and geodynamics under the Middle Qinling Mountains (MQL) and the Dabashan Thrust Belt (DBTB) on its southern flank (Dong et al., 2013; Ren et al., 2012; Teng et al., 2014a, 2014b; Wang et al., 2014). The present work addresses a comprehensive gravity study that is added to other previous geophysical studies based on wide-angle seismic reflection/refraction soundings (Teng et al., 2014a, 2014b), teleseismic receiver functions (Si, 2015; Si et al., 2016) or a geomagnetic survey (Hu et al., 2014).

With the purpose of characterizing the complex crustal structure under MQL and DBTB (to the south) and the Ordos Basin (to the north), as well as the interaction between the North China Block and the South China Block, a 1000-km-long south-to-north gravity profile was performed in 2011 along the line Yuquan-Xi'an-Yan'an-Yulin (line A-A′ in Fig. 1), which goes from the Sichuan Basin to the Ordos Basin across Dabashan, Qinling and the Weihe Graben. In this paper, available seismic data are combined with new gravity data, and the density structure and isostatic equilibrium state of the crust along the reference profile is studied. Finally the geodynamic implications are discussed.

2. Tectonic setting

The profile A-A′ (Fig. 1) runs across the five major tectonic units that make up the study area, namely (from south to north): Sichuan Basin (SCB), Dabashan Thrust Belt (DBTB), Qinling Orogen (QLO), Weihe Graben (WHG) and Ordos Basin (OB). SCB is roughly circular and contains mainly Paleozoic and Mesozoic sedimentary rocks that are bordered by Cenozoic formations on the southern margin, which are merged westward and northward in Longmen Shan (Burchfiel et al., 2008). There are folded belts of the Late Triassic-Cretaceous to the north and the Late Cretaceous to the east. The basement of the basin has remained relatively undeformed or stable during the Mesozoic and Cenozoic deformation episodes that affected the surrounding regions (Burchfiel et al., 2008).

DBTB is a curved tectonic belt located in the transition zone between SCB and QLO, which was formed as a result of the collision between the Qinling Orogen and the South China Block during the Late Triassic (Hu et al., 2012; Li et al., 2013, 2015). Generally, this belt is characterized by southwestward thrusting kinematics, representing the propagation of an orogenic belt toward the foreland (Li et al., 2012). DBTB limits with QLO to the north through the Ankang fault and with SCB to the south through the Tiexi fault (Shi et al., 2012, 2013); the formation is crossed by the Chengkou fault that separates two petrotectonic units called southern and northern DBTB (Zhang et al., 2010b; Shi et al., 2012, 2013). These two belts have complex structures along the transverse and longitudinal directions (Dong et al., 2011a, 2011b; Li et al., 2012; Shi et al., 2012, 2013).

The geological framework of QLO was built by the interaction of three blocks, namely: North Qinling, South Qinling and the South China Block, separated by the Shangdan and Mianlue sutures (Meng and Zhang, 2000). QLO has experienced a prolonged divergence and convergence between blocks (Zhang et al., 1996). During the period between the Late Neoproterozoic and the Early Paleozoic, South Qinling was the northern margin of the South China Block, while North Qinling was the southern margin of the North China Block, both formations separated by the Proto-Tethyan Qinling Ocean. North Qinling evolved into an active margin on the occasion of the northward subduction of the Proto-Tethyan Qinling Ocean during the Ordovician period. The collision between South and North Qinling took place in the Middle Paleozoic along the Shangdan suture. Synchronously with this collision, it occurred rifting on the southern border of South Qinling, which was followed by the opening of the Paleo-Tethys Ocean during the Late-Paleozoic and the splitting of the South China Block from South Qinling. The collision between South Qinling and the South China Block

happened along the Mianlue suture in the Late Triassic. This Late Triassic collisional orogeny caused extensive fold-and-thrust deformation and granitoid intrusions throughout Qinling, and led to the final joining of the North and South China Blocks (Dong et al., 2011a, 2011b, 2013; Meng and Zhang, 1999, 2000; Zhang et al., 1995, 1996).

The Weihe Graben is the coupling zone between QLO and OB. WHG was dominated by the far-field effect of the India-Eurasia collision, which gave rise to a significant extension and subsequent thinning of the crust during the Cenozoic (Peltzer and Tapponnier, 1988; Wang et al., 2014; Zhang et al., 1998). WHG started to develop in the Mid-Late Eocene and is filled of a thick sequence of lacustrine and alluvial deposits covered by Quaternary loess (Zhang et al., 1998). During the Mid-Late Miocene, the subsidence extended to the whole area and increased abruptly to a rate of about 0.20 mm/yr, i.e. four times faster than in the previous period (Zhang et al., 1998), so that the sediments deposited during this geological period reach a thickness of 2500 m (Zhang et al., 1998). During the Quaternary period, the subsidence increased to a rate of about 1 mm/yr in the axial depressions where Quaternary deposits exceed 1000 m.

Lastly, OB is located in the western part of the North China Block and is currently considered as a topographic plateau. It is a stable sedimentation cratonic basin (Yang, 2002) with internal characteristics of rigidity and heterogeneity (Jia and Zhang, 2005). OB developed faults in rectangular blocks in the Paleozoic and much later the basin was cut by a system of adjacent faults in the Cenozoic (Zhang, 1989; Liu et al., 2006). The formation behaves like a stable block surrounded by active tectonic belts.

3. Gravity data

3.1. Data acquisition and gravity reductions

The gravity dataset that we use in this study comes from the already mentioned north-south 1000-km-long profile across MQL and the near blocks (as is shown in Fig. 1, line A-A′), which was performed between March and June in 2011. This profile extends from Yuquan in the south, crosses Xi'an and Yan'an, and ends at Yulin in the north. In the course of the fieldwork, two Lacoste & Romberg model G gravimeters (No. 596 and No. 1149) with resolution of 0.01 mGal and accuracy of 0.08 mGal were used. The measurement points were selected to facilitate the exploratory practice, i.e. in relatively flat and easily accessible terrain conditions, to have accurate GPS locations and gravity reductions with the least possible error. A total of 1116 gravity measures were collected in so other many observation points, covering a distance of 1010 km perpendicular to the strike of the main tectonic formations.

Once the raw gravity data were collected, the following reductions were practiced to obtain the correct gravity value and furtherly the Bouguer gravity anomaly (hereafter BGA) along the reference profile: (1) earth tide reduction; (2) free-air reduction; (3) mass reduction (assuming a density value of 2.67 g/cm^3); (4) topographic reduction (with density of 2.67 g/cm^3 and for distances from 0 km to 167.7 km); (5) normal reduction using the GRS80 Geodetic Reference System (Moritz, 1980) as reference ellipsoid, then incorporated into the WGS84 World Geodetic System (Jacoby and Smilde, 2009). After all these corrections, the gravity anomaly was estimated with rms accuracy of 0.3 mGal.

3.2. Topographic relief and Bouguer gravity anomaly

The goal of our study is the crustal structure and dynamics in the Middle Qinling Orogen and nearer tectonic units, so we focus our attention on a latitude range between 31°N and 36°N (transect B-B′ in Fig. 1) that comprises the north part of SCB and the south part of OB. Fig. 2 shows both the topographic heights and the Bouguer gravity anomaly along the B-B′ transect. As can be seen BGA varies strongly within a range from -110 mGal to -200 mGal along the B-B′ segment and reveals remarkable differences among the tectonic units that form the study region: (1) In the south end of the profile, northern part of SCB (31°N–31.8°N), the topographic elevation increases from 500 m to 1200 m, while BGA decreases gradually from -120 mGal to -150 mGal near 31.8°N. (2) In the stretch of DBTB (31.8°N–33.0°N), BGA changes rhythmically with the topographic relief; thus, along with increasing elevation of topography, BGA also increases from −145 mGal near 31.8°N to -110 mGal near 32.6°N, and then decreases to −145 mGal near 33.0°N, with a sharp gravity gradient of 80 mGal/100 km. (3) Further north, in the stretch of MQL (33.0°N–34.0°N), the topographic elevation increases abruptly from 400 m on its south margin to 2250 m of the main peak in MQL near 33.8°N, and then again decreases to 400 m on its northern margin. While BGA keeps mirror symmetry with the topographic elevation and decreases from -140 mGal near 33.0°N on the southern margin of the Qinling Mountains to -180 mGal near 33.6°N at the center of MQL, and then increases to -150 mGal on the northern margin of MQL. After these oscillations the gravity anomaly decreases very sharply to −195 mGal on the southern margin of WHG. (4) In the stretch of WHG (34.0°N–34.8°N), the topography is rather flat and ranges from 400 m to 700 m, although most of the heights are between 400 and 500 m; but BGA increases progressively from −195 mGal on the south margin to −130 mGal on the northern part with an average gradient of 85 mGal/100 km. (5) In the southern part of OB (34.8°N–36°N), the topographic elevation increases from 700 m to the highest value of 1500 m, and BGA varies symmetrically with the elevation in a small range between −130 mGal and −150 mGal.

Fig. 3 shows the Bouguer gravity anomaly vs. topographic elevation for the different tectonic units that make up the study region. The BGA-topography relationship changes for different tectonic belts. The correlation of BGA with the irregular topography along the B-B′ segment (Fig. 1) allows us to conclude that both the physical structure and the isostatic equilibrium state of the crust are key issues for the understanding of the evolution and geodynamics affecting the study area.

4. Seismic velocity and density across MQL

4.1. P-wave velocity model

The seismological information is based on a 1000-km-long wide-angle seismic reflection/refraction profile performed across OB, WHG, MQL, DBTB and SCB, which was conducted by Teng et al. (2014a) (Fig. 1). Up to 9 shot points were fired at different sites approximately every 100 km. For each shot, a series of closely spaced boreholes were drilled and loaded with 1320–3801 kg of dynamite. A total of 492 portable seismometers were used to get record sections along the 1000-km-profile at intervals of 2 km on average. Based on the interpretation of the reflection/refraction seismic phases, we constructed a two-dimensional P-wave velocity model for the crust and upper mantle that we show in Fig. 4. The accuracy of the final velocity model depends on several factors, namely: the shot point spacing and the number of receivers, the ray density and the correct identification of the different seismic phases. In general, seismic velocity determinations have fewer errors than depth determinations. Considering the seismic data compiled from this profile, the seismic velocities are accurate within 3%, i.e. within an error band of ± 0.2 km/s as maximum; while the depths of the inner interfaces, including the Moho, are accurate within 10% depth (Mooney and Braile, 1989).

The Moho depth varies smoothly between 42 and 45 km in SCB (south segment of the line A-A′) and OB (north segment of the line A-A′). The Moho sinks about 3–4 km below DBTB and south pat of MQL, and rises strongly about 10 km below WHG where the crust is less thick than through the whole profile. The crust is divided into two layers: the upper crust with a sedimentary cover and the lower crust, both separated by an interface identified by the P2 phase observed in the seismic records and labelled as C2 in Fig. 4, which is identified as the Conrad discontinuity. There are also two other intra-crustal interfaces: one

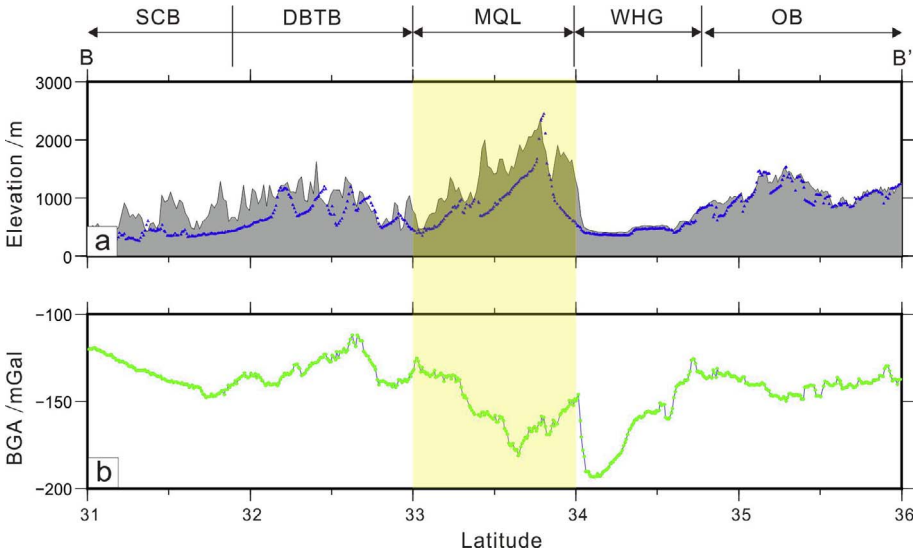

Fig. 2. Rugged topography (a) and Bouguer gravity anomaly (b) along the transect B-B′ (Fig. 1). The blue triangles in the upper plot indicate gravity measurement points. The vertical band in yellow color covers the extension of MQL in north-south direction. Acronyms are the same as in Fig. 1. (For interpretation of the references to color in this figure legend, the reader is referred to the web version of this article.)

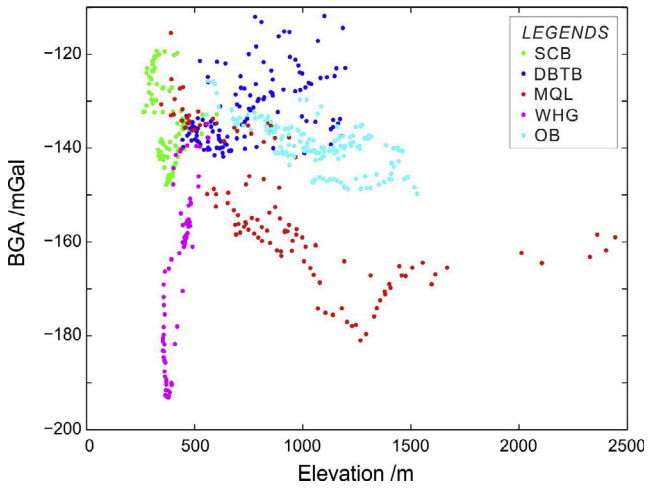

Fig. 3. Bouguer gravity anomaly vs. topographic elevation of the different tectonic units that make up the study region. Data points appear in distinct colors for an easier understanding of the information. Acronyms (top right corner) are the same as in Fig. 1.

lying in the upper crust above the previous discontinuity, south of WHG, labelled as C1 (given by the P1 phase in the seismic records), and another in the lower crust under the northernmost section of the profile A-A′, labelled as C3 (given by the P3 phase in the seismic records). The thickness of the sedimentary cover ranges from 0 to 8 km and the P-wave velocity varies widely from 2.6 km/s to 5.5 km/s. In general, there is a good agreement between near-surface speeds and shallow geological formations. Relatively high speeds coincide with zones where the basement is near the ground surface, and low speeds are clearly associated with the presence of sedimentary basins. The bottom of the upper crust reaches the depth of 22.7 km in WHG, although it varies slightly around 28.5 km beneath SCB and 25.0 below OB. P-wave velocity values range from 5.6 km/s to 6.3 km/s in the upper crust. The thickness of the lower crust varies between 13 km beneath WHG and 25 km beneath OB. Below the upper crust, the P-wave velocity increases abruptly to 6.5 km/s and takes values of 6.8–7.0 km/s at greater depths near the Moho discontinuity. The interface C3 at an average depth of 35.5 km in the lower crust only exists at the northernmost transect of the profile. Under the Moho in OB, a weak reflection interface (denoted by the capital letter L in Fig. 4) could also be identified at 65–68 km depth by following a reflection seismic phase close to the Pn phase.

4.2. Reference density model

In order to obtain the crustal density structure model, a starting model was initially constructed based on different types of information: (1) in those areas with outcrops, it is referred to the average density

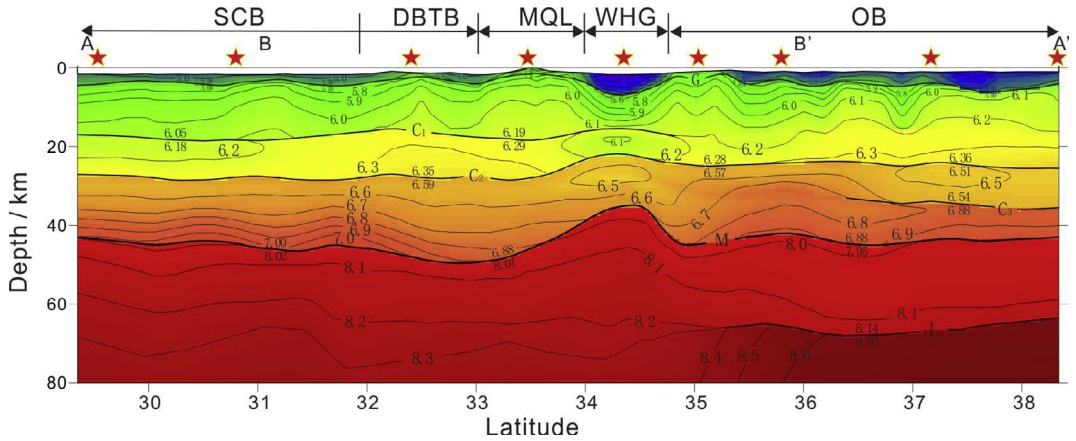

Fig. 4. Velocity model along the profile A-A′ (Fig. 1) obtained from the wide-angle seismic reflection/refraction sounding (Teng et al., 2014a). The red stars mark the locations of the shot points fired in the course of this sounding. Acronyms are the same as in Fig. 1. (For interpretation of the references to color in this figure legend, the reader is referred to the web version of this article.)

values of the exposed rocks; (2) in areas lacking outcrops or in other depth zones, P-wave velocities (Teng et al., 2014a, 2014b, Fig. 4) were converted into densities in agreement with accredited velocity-density relationships and previous geological information. In general, the densities of sedimentary rocks are affected by composition and porosity, and increase with the age of the rocks. The densities of magmatic rocks are controlled by the content of dark mineral, and increase from felsic to mafic rocks; the average density is 2.56–2.62 g/cm^3 for granitoid rocks, 2.60–2.70 g/cm^3 for intermediate or felsic intrusive rocks, and 2.82–3.32 g/cm^3 for mafic and ultra-mafic rocks. The densities of metamorphic rocks are higher than those of the origin rocks (Wang et al., 2010). To date, several mathematical correlations between seismic P-wave velocity and density have been tested in many laboratories and field experiments on the elastic properties of rocks (Christensen and Mooney, 1995; Deng et al., 2014; Feng et al., 1986; Ludwig et al., 1970; Nafe and Drake, 1957; Zhang et al., 2008b; Zhao et al., 2013). In this study, the initial density model was constructed from P-wave velocity using the empirical velocity-density relationship given by Eq. (1), which is based on statistical results of velocity and density and is confirmed as a valid relationship for the determination of crustal density in China (Feng et al., 1986):

$$\rho = \begin{cases} l2.78 + 0.56(v_p - 6.0) \ldots\ldots (v_p \leqslant 6.0) \\ 3.07 + 0.29(v_p - 7.0) \ldots\ldots (6.0 < v_p \leqslant 7.5) \\ 3.22 + 0.20(v_p - 75) \ldots\ldots (v_p \geqslant 7.5) \end{cases} \quad (1)$$

4.3. Modeling the density distribution

The interactive modeling of the gravity field on a two-dimensional polygonal cross-section in a spatially uniform environment allows us to obtain theoretically the density structure of the target area (Artemjev et al., 1994; He et al., 2014; Tiwari et al., 2006; Zhang et al., 2010a, 2010c). In this study we used the software "Gm2dInverse" developed by the Research and Development Center of the China Geological Survey. The inversion and modeling of gravity data depends to a great extent on the known geological characteristics and on the information provided by other previous geophysical studies on the explored region. Measured physical parameters of rock samples and surface geology are valuable constraints that can reduce greatly the non-uniqueness of the solution. The interactive simulation procedure can be summarized as follows: (1) construction of an initial structure model on the basis of the available geological information on tectonic units and main tectonic boundaries; (2) introduction of the known physical parameters of deep structures provided by geophysical surveys; (3) calculation of the theoretical gravity anomalies starting from the initial model; (4) comparison of these theoretical gravity values with those measured directly in the field to decide if the model needs revision or updating; (5) if the result of this comparison is rather poor, the initial model must be revised and the above steps have to be repeated up to obtain an acceptable fit between measured and calculated data; (6) the best-fitting model is taken as the final result for the interpretation of detected anomalies (He et al., 2014; Zheng et al., 2009).

4.4. Final density model

Taking the initial density model as reference, we proceeded to an iterative updating until the most adequate model was able to explain the observed gravity anomalies. Fig. 5b shows the 2-D density model of the crust beneath the B-B′ transect. It can be seen a blocky and horizontally layered structure which provides us basic information on the crustal properties, rheology and dynamics beneath MQL and the adjacent areas. Although there are several studies that, from the viewpoint of tectonics and surface geology, focus on the formation of the Qinling Orogen through the collision between the North China Block and the South China Block (Mattauer et al., 1985; Sengor, 1985; Zhang et al., 1996, 2001; Meng and Zhang 1999; Faure et al., 2001; Ratschbacher et al., 2003, 2006; Dong et al., 2011a, 2011b, 2012, Dong and Santosh, 2016), the fact is that the fine density structure that correlates with collision episodes has remained unclear to date. The density model for MQL gives us the opportunity to investigate not only the regional architecture, but also the dynamics, including the state of isostatic compensation and the delamination of the lower crust.

4.5. Error analysis

The fit between the observed and calculated gravity anomalies strongly supports the reliability of the results (Deng et al., 2014). Fig. 5a shows the predicted anomalies of Bouguer gravity as well as the fit between observed and calculated anomalies estimated from the density model. Fig. 5c shows the discrepancy (misfit) between both gravity anomalies. The observed mismatch does not exceed 2.0 mGal in the transects south of 32°N (SCB) and north of 35°N (OB) and is less than 5.0 mGal in the mid-section of the profile (MQL and WHG) where there is a remarkable variation in gravity (Fig. 5a) because of the non-homogeneous upper crust (Fig. 5b) and the complex topography (Fig. 2a). The standard deviation obtained through gravity modeling is only 1.26 mGal and there are no regional trends. As a whole, the gravity field calculated by forward modeling from the density distribution model correlates well with the observed gravity field along the entire profile. Thus, the density structure obtained in this study allows us to successfully reproduce the gravity measurements collected along the profile. As can be seen, all the main features of gravity seem to be well recovered and the gravity field values agree with the observed ones, with the highest value being about −110 mGal and the lowest value of -200 mGal.

4.6. Density of the sedimentary cover

Fig. 6b shows an overview of the 2-D density structure of the crust and uppermost mantle and also the interfaces delimiting the main layers of the crust; while Fig. 6a shows several 1-D density-depth profiles at some sites (whose respective latitudes are indicated in the illustration) located in different tectonic environments. At the most superficial part of the crust, the density exhibits a large vertical gradient and rapidly increases from 2.5 g/cm^3 to 2.65 g/cm^3. The reason for this density gradient in the sedimentary cover may be the existence of not fully closed pores in unconsolidated layers subjected to low pressure. Since the density is generally higher than 2.65 g/cm^3 in the crystalline crust (Segev et al., 2006), this value is considered the limit for drawing the dividing line between the sediment layer and the crystalline crust (red line in Fig. 6b). The sediment thickness ranges from almost zero in DBTB and MQL to approximately 10 km in WHG. The crystalline basement varies smoothly in SCB and OB where it has an average depth of 2 km and 4 km, respectively. WHG has not only the thickest sedimentary cover with a maximum thickness of 10 km, but also the lowest density values of 2.33–2.43 g/cm^3 on average. Based on our own results and also on previous geological research (Peng et al., 1992; Zhang et al., 1998), the relatively low BGA observed in WHG is due to the large amount of low density materials accumulated in a so thick sediment layer. The rather smooth crystalline basement observed in OB and SCB could be the result of a stable sedimentary process during the Cenozoic period.

4.7. Density of the crystalline crust

In the crystalline crust, the density slowly increases with depth from 2.65 g/cm^3 to the highest value of 2.95 g/cm^3 near the bottom of the crust (Fig. 6b). The Conrad interface, which separates the upper crust from the lower crust, varies smoothly within a depth range of 22–32 km along the entire B-B′ transect (blue line in Fig. 6b). The determination of this discontinuity is based on seismic velocities and gravity data

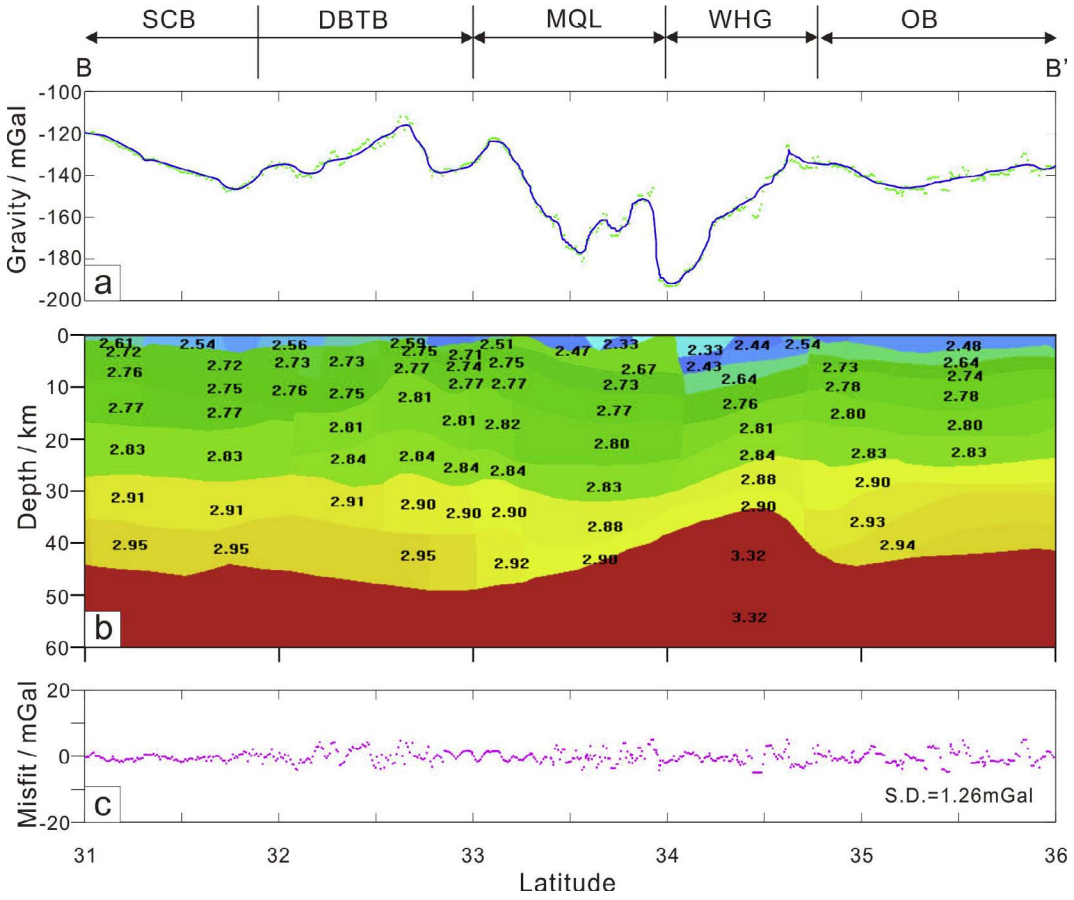

Fig. 5. Crust/upper-mantle density structure across the gravity profile B-B′ (Fig. 1). (a) Fit between measured Bouguer gravity anomaly (green dots) and calculated gravity anomaly (blue line) from the density model; (b) 2-D crust-mantle density model obtained by gravity data inversion; (c) Discrepancy between measured and calculated gravity anomalies (standard deviation of 1.26 mGal). Acronyms are the same as in Fig. 1. (For interpretation of the references to color in this figure legend, the reader is referred to the web version of this article.)

obtained previously. As already mentioned, the reflection seismic phase P2 is the one that defines the interface labelled as C2 (Fig. 4) that we identify as the Conrad interface (CI in Fig. 6b). A density jump of about 0.05 g/cm^3 can be observed on both sides of CI (Fig. 6a-b) when entering into the lower crust, which is in agreement with the velocity model of Teng et al. (2014a) (Fig. 4). Going northward, CI deepens and reaches a depth of 28 km beneath the southern margin of MQL, which becomes 32 km in its northern margin, the latter being the deepest level of CI along the whole profile. In WHG, CI rises from 28 km to 23 km, and then maintains steady at about 25 km in OB. The average density of the crust in MQL is clearly lower than the density on both sides. From MQL to the boundary between WHG and OB, the lower crust is gradually thinner; this specific feature of the crust can be correlated with the evolutionary history of QLO and naturally with the collision between the South China Block and the North China Block.

4.8. Undulation of the Moho

The Moho depth (green line in Fig. 6b) varies in the range of 33–49 km along the B-B′ segment (Fig. 1). Underneath SCB the Moho varies within a small range from 44 km to 46 km and below DBTB the Moho deepens northward from 45 km to 49 km, which is the greatest depth that it reaches near the boundary between DBTB and MQL and also the largest along the whole profile. An interesting finding is that below the MQL orogenic belt, the Moho rises gradually from 49 km on the southern margin to 38–40 km on the northern margin, and farther north reaches its lowest depth of 33 km beneath WHG. In the north part of the B-B′ transect, the Moho undulation is similar to that existing in SCB, within a depth range from 42 km to 45 km, in correspondence with the stable evolution of the North China Block and the South China Block. The Moho in WHG can be explained by tectonic extension caused by upwelling of mantle materials. But the Moho in MQL, which roughly reflects the topography elevation of the zone, reveals a peculiar undulation that can be attributed to the geodynamic evolution of the lower crust in this area.

5. Isostatic state of the crust

5.1. Airy and Pratt isostatic compensation models

The isostatic compensation state of the crust is a key issue in the context of the regional geodynamics, but the way in which equilibrium is achieved remains a topic of lively debate. Regional and residual isostatic anomalies based on observed gravity anomalies and correlation with the major tectonic provinces may shed light on the crustal thickness variations and the most relevant density anomalies in the crust (Aitken, 2010; Ussami et al., 1993), structural zoning (Burov et al., 1990; Lyon-Gaen and Molnar, 1984; Tiwari et al., 2006), and crustal movements (Fu et al., 2014; He et al., 2014; Jordan and Watts, 2005; Zhang et al., 2014). For these reasons, for many decades, the analysis of the isostatic state of the crust has generally been carried out with the help of the classical Airy or Pratt models to study the continental geodynamics (Jacoby and Smilde, 2009).

The basic idea of the theory of isostasy is that if we imagine many vertical straight prism-shaped blocks form the crust, all these blocks will have the same weight above a compensation level according to the principle of hydrostatic equilibrium. The difference between the classical Airy and Pratt models lies on the geometry of the compensation

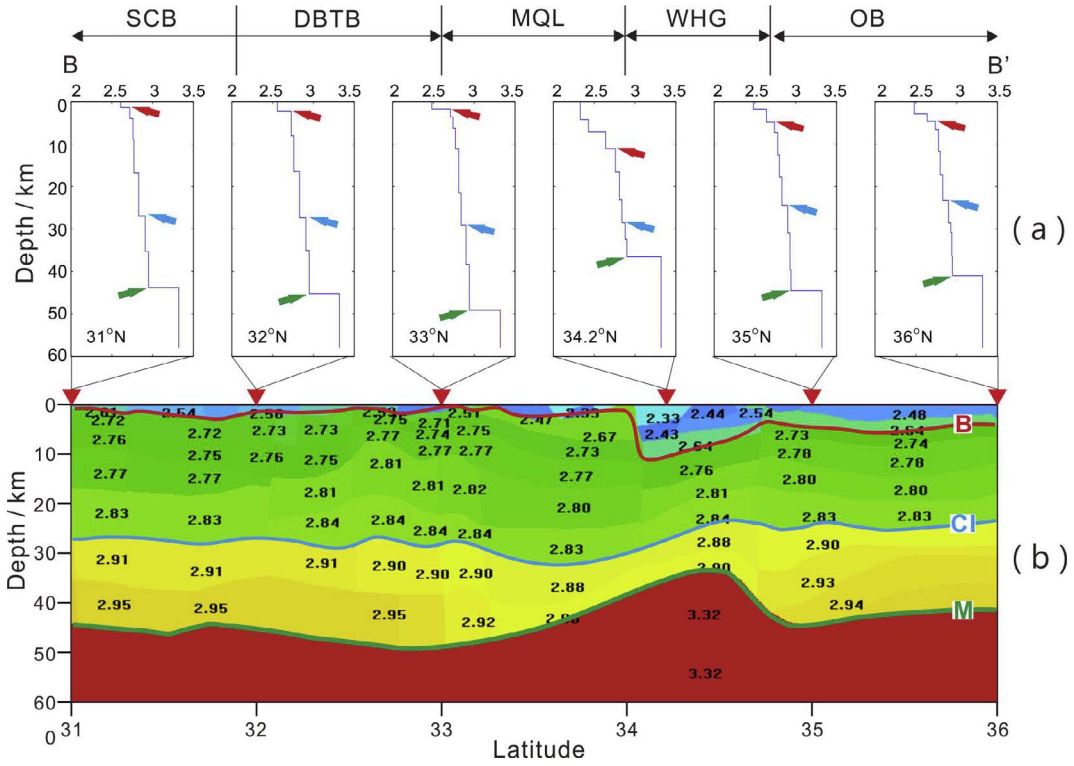

Fig. 6. Layering of the crustal density model along the gravity profile B-B′ (Fig. 1). (a) 1-D density-depth profiles at different sites identified by their latitudes; the red, blue and green arrows in each panel indicate the locations of the crystalline basement, Conrad discontinuity and the Moho, respectively. (b) 2-D density model of the crust with interfaces separating the main layers; the red, blue and green lines delimit the crystalline basement (B), Conrad interface (CI) and the Moho discontinuity (M), respectively. (For interpretation of the references to color in this figure legend, the reader is referred to the web version of this article.)

level, assimilated to the sinking of the Moho (Turcotte and Schubert, 2002; Watts and Burov, 2003). In the Airy model the crustal and upper mantle densities (ρ_c and ρ_m respectively) are assumed to be constant, so that the Moho depth is laterally variable due to the overload of the topographic mass lying above the geoid (Fig. 7a). On the contrary, in the Pratt model all the vertical rectangular prisms that form the crust have different densities, so that all blocks weigh the same above the compensation level that now is flat everywhere (Fig. 7b). Both the Airy and Pratt models are based on ideal assumptions in which the Earth's crust is considered a really simple structure and, therefore, none of these models is a suitable scheme to accurately model the true isostatic state of the crust.

Hence, to investigate the isostatic equilibrium state of the crust in MQL and adjacent areas with greater reliability, a new combined isostatic compensation model, called Airy-Pratt model or "A-P model", was proposed, which takes advantage of the Airy and Pratt's hypotheses. In the A-P model (Fig. 7c), each crustal column, denoted generically by the subscript k (k = 1, 2, 3, …), is divided into several vertical prisms each with its density (ρ_{k1}, ρ_{k2}, …,ρ_{knk}) and height (h_{k1}, h_{k2}, …, h_{knk}), thus reproducing the variations in density of the crust both vertically and laterally according to the established density model. With this notation, n_1 is the number of layers (prisms) for the block I_1, n_2 is the number of layers for the block I_2, and n_k is the number of layers for the k-th prismatic block I_k. In this way the density distribution can be projected onto the A-P model without any simplification or loss of accuracy.

When calculating the isostatic state of the crust using the A-P model, we assume that the pressure P_k caused by the k-*th* prismatic block I_k on the compensation level E-E′ is (Fig. 7c):

$$P_k = \sum_{i=1}^{n_k} g\rho_{ki}h_{ki} + g\rho_m t_k \tag{2}$$

In this equation, the first term on the right side is the accumulated pressure on account of each prism inside a specific crustal block, while the second one is the pressure due to the prismatic column of the upper mantle; g is the acceleration of gravity; ρ_{ki} is the density of the i-th prism inside the k-th prismatic block I_k of the crust and h_{ki} is its thickness; ρ_m is the upper-mantle density; and t_k is the thickness from the bottom of the k-th prismatic block down to the Moho. Assuming hydrostatic equilibrium, the pressure P_k exercised by the material column or vertical block I_k on the compensation level E-E′ will be the same as the pressure due to other columns, i.e. the standard pressure P_s:

$$P_1 = P_2 = P_3 = \ldots\ldots = P_k = P_S \tag{3}$$

For any prismatic block in equilibrium, if we know the Moho depth and the density distribution in the crust, we can calculate the pressure P_s on the level E-E′ below the Moho and hence the thickness t_k, i.e. the thickness of the upper mantle column between the Moho and E-E′. Combining Eqs. (2) and (3), we have

$$t_k = \frac{P_S - \sum_{i=1}^{n_k} g\rho_{ki}h_{ki}}{g\rho_m} \tag{4}$$

Consequently, we can determine the theoretical depth D_k of the Moho beneath each prismatic column under the condition of an isostatically compensated crust. If we take T as the depth from the geoid to the isostatic compensation level E-E′ (Fig. 7c), D_k can be expressed as

$$D_k = T - t_k \tag{5}$$

The isostatically compensated Moho depth (D) is that of the crust when it has reached the isostatic equilibrium, which has geodynamic implications when compared to the Moho depth (M) based on the density model. According to the theory of isostasy, the D and M depth values must be equal when the crust is in isostatic equilibrium.

The Yulin area in the Ordos Basin is taken as the reference region, since it is generally accepted that here the crust is stable and is in isostatic equilibrium state. The depth of 60 km is set for the compensation level E-E′, because the Moho never exceeds 60 km depth along

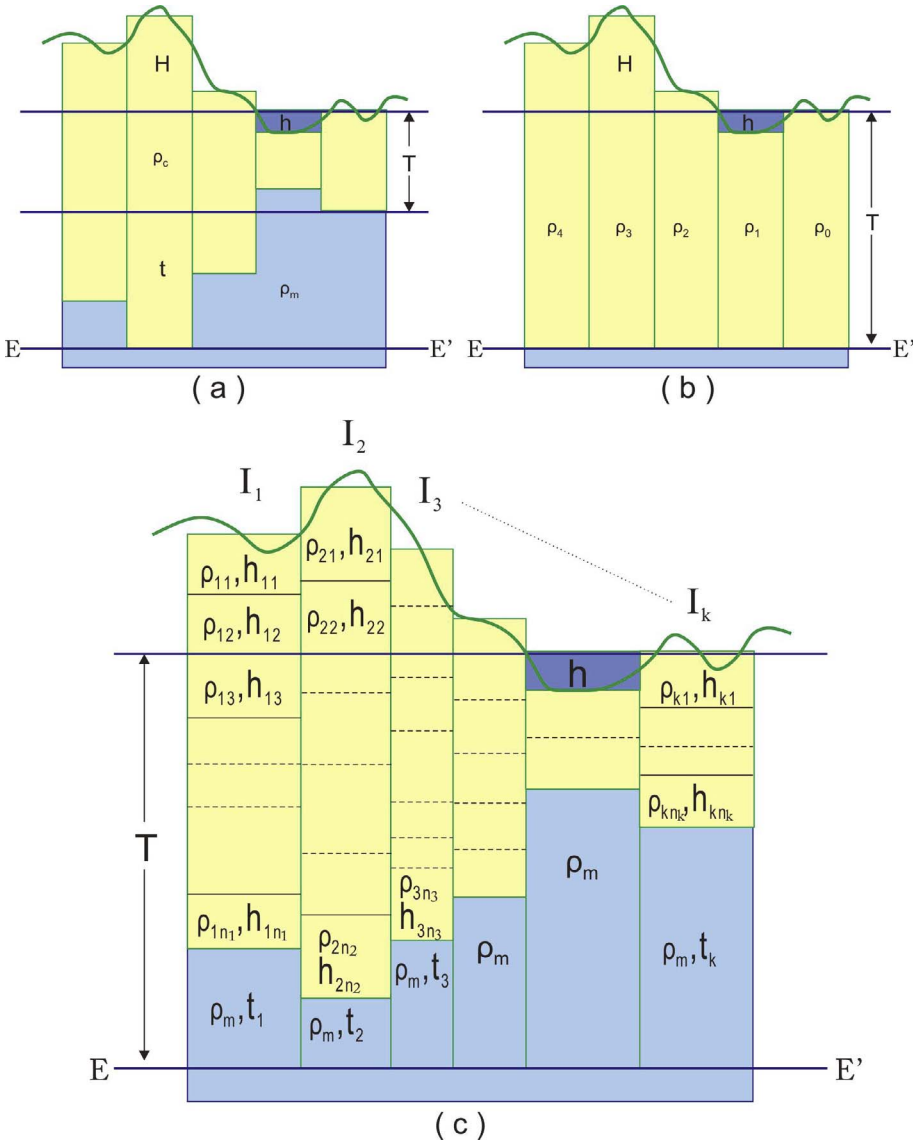

Fig. 7. Schematic illustration of the Airy and Pratt isostatic compensation models and the Airy-Pratt combined model. (a) Airy model: ρ_c is crustal density; ρ_m is mantle density; H is elevation above the sea level; h is depth below the sea level; *t* is the crustal root thickness; T is the average thickness of the isostatically compensated crust. (b) Pratt model: ρ_0, ρ_1, ρ_2, etc., are the respective densities of the blocks that make up the crust, which are isostatically compensated on the same level of equal depth (E-E′); T is the thickness going from the sea surface down to the common isostatic compensation level. (c) Airy-Pratt model: t_k is the thickness from the base of the k-th prism I_k down to the Moho; ρ_{ki} is density of the k-th prismatic block that forms the prism I_k of the crust, and h_{ki} its thickness; T is the depth going from the geoid surface down to the isostatic compensation level E-E′.

our survey line, so that all the crust/mantle prisms are supposed to be isostatically compensated above this depth level (T = 60 km). Having substituted the density values of the crust in Yulin in Eqs. (2) and (3), we obtain P_s = 1730 MPa. From here, admitting the fulfillment of equalities (3) and considering the crustal density model along the B-B′ transect, it is possible to calculate the Moho depth D by Eqs. (4) and (5) to compare it with the Moho depth M obtained earlier from the gravity and density data. Fig. 8a shows these results concerning the Moho depth.

5.2. Comparison between isostatic and observed depth of the Moho

The comparison between the isostatic Moho depth D and the Moho depth M can help to reveal whether or not the crust is in isostatic equilibrium and to predict the movement of the crust. If the crust is isostatically compensated, then D = M. If D < M, the crust has not yet reached the equilibrium (Fu et al., 2014; Zhang, 2013; Zhang et al., 2010c, 2014) and must rise (together with the topography) to reach the equilibrium. In the course of this process, the crustal thickness (from ground surface to the Moho) will not change, but M will be somewhat less deep accompanying the topography elevation. Hence, the value of M will be closer to that of D. Under this condition the load of the crustal material will be supported by some other mechanism such as the flexural strength of the lithosphere (Fu et al., 2014; Jordan and Watts, 2005). Isostasy can therefore be understood as a way of studying the dynamic process that governs the movement of crustal blocks (Fu et al., 2014; Mooney and Vidale, 2003; Zhang, 2013; Zhang et al., 2010c, 2014).

Fig. 8a shows the two (dotted) curves depicting the Moho depth (D and M), which have been obtained by different ways, as well as an overall view of the discrepancy between them (Fig. 8b). As can be seen, the D and M values are comparable in default of a small difference of 0.2 km on average and less than 0.4 km in the SCB and OB areas. The largest discrepancy is found in MQL, where it is 0.8 km. Given that the discrepancy between D and M is not sufficiently large, we cannot conclude the isostatic state of the study area from the calculation based on the A-P compensation hypothesis. Now, assuming no miscalculations have been made and discarding the unrealistic assumption that MQL has remained stable as an inactive tectonic region for a long time, the alternative interpretation is that the crust in MQL is not fully compensated. Considering the complex tectonics (Dong et al., 2004, 2011a, 2011b, 2013; Li et al., 1996; Meng and Zhang, 1999, 2000; Zhang et al., 1995, 2001), the multi-phases orogeny (Mattauer et al., 1985; Meng and Zhang, 1999, 2000; Ratschbacher et al., 2003, 2006; Zhang et al., 1995, 1996) and the Bouguer gravity anomaly vs. topographic elevation (Fig. 3), we think this interpretation of the isostatic equilibrium in

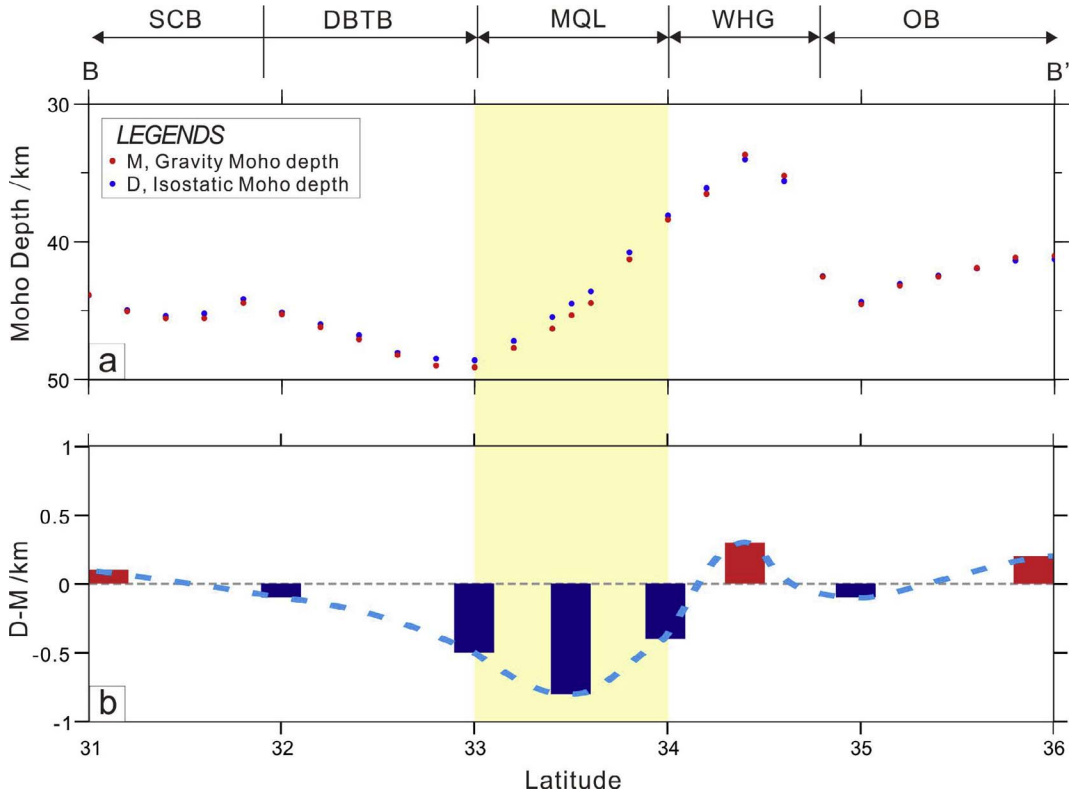

Fig. 8. (a) Difference between the Moho depth when the crust has reached the isostatic equilibrium state (D) and the Moho depth once inverted from gravity data (M), along the gravity profile B-B′ (Fig. 1). (b) Discrepancy values between M and D. The vertical band in yellow color marks the position of MQL. Acronyms are the same as in Fig. 1. (For interpretation of the references to color in this figure legend, the reader is referred to the web version of this article.)

MQL is the most plausible.

6. Discussion

6.1. Rheology of the crust

The density values increase with depth more rapidly above CI than below (Fig. 6b), whereby the upper crust is often considered to be composed of brittle material whose physical properties undergo a clear change with a large vertical gradient; while the lower crust is often considered to be composed of ductile or plastic material whose physical properties vary to a lesser extent. The spatial location of the earthquake hypocenters is the cornerstone for examining the rheology of the crust (Maggi et al., 2000; Watts and Burov, 2003). Fig. 9 shows the distribution of the seismic foci in the explored region, according to the earthquake catalogs of the China Earthquake Network Center. All seismic events have magnitude Ms > 2.5: more than 90% of these foci occurred in the upper crust beneath the crystalline basement, but only a few of them in the lower crust; which is consistent with the global pattern of that most earthquakes with hypocenter in the continental lithosphere occur in the upper crust, while the lower crust is partially or even completely aseismic (Chen and Molnar, 1983; Chen, 1988). Given the fact that earthquakes occur mainly in a faulting environment with fragile rocks at low temperature, and considering the aforementioned change in the vertical density gradient, it is obvious that CI behaves as a rheological transition zone that separates the brittle crust from the ductile crust. We also note a gap or lack of seismic events right in the transition zone between MQL and WHG which again relates to the

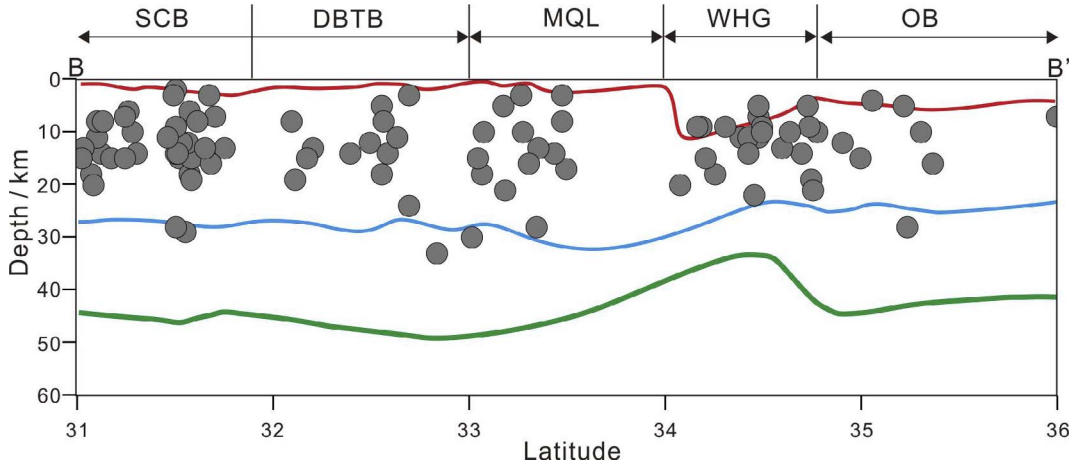

Fig. 9. Spatial location of earthquake hypocenters in the crust underlying the gravity profile B-B′ (Fig. 1). Acronyms are the same as in Fig. 1.

orogeny of these tectonic units and seems to indicate not only the collision front between the South China Block and the North China Block, but also an increase of the stresses in the zone.

6.2. About the existence of a root beneath MQL

The Moho discontinuity, which is the natural boundary between the crust and the mantle lithosphere, plays a key role in the evolutionary history of the continental crust. The style of the Moho is the response to the geodynamic processes undergone by the crust. When constructing the crust density model for the study area, we can approach the formation and properties of the Moho interface from the dual perspective of the knowledge of the gravity field and the density distribution.

The existence of a "mountain root" is a common feature of the lithosphere worldwide when young orogens are in collision (Artemieva and Meissner, 2012). According to previous geophysical research, the Moho depth varies between 29 and 37 km with an average depth of 34 km beneath the East Qinling Orogen (Gao et al., 1999; Yuan et al., 1994), which is obviously less than the average estimation of 37–40 km for the global Moho depth (Christensen and Mooney, 1995; Rudnick et al., 1995) and implies a loss of crustal root. However, the Moho beneath the West Qinling Orogen is as deep as 51 km (Gao et al., 2014; Wang et al., 2007; Zhang et al., 2008a), thus suggesting the opposite (Wang et al., 2013). According to the seismic study conducted by Teng et al. (2014a) and this gravity study, the Moho depth in MQL varies from 49 km on the southern margin to 38 km on the northern margin. These latter depth values are among the characteristic ones of East Qinling and West Qinling, so it is possible to speculate about the existence of a weak root beneath MQL, even though its thickness would not be as great as in West Qinling.

In addition, as we have seen, the theoretical Moho depth (D) in QLO predicted by isostasy is lower, up to 0.8 km, than the Moho depth (M) based on the crustal density model (Fig. 8b). From the viewpoint of the isostatic equilibrium, this implies that the crust below MQL is not yet fully compensated. It can then be speculated that the crust will still undergo a progressive lifting in MQL up to reach steady state, in contrast to the Ordos and Sichuan basins that will remain stable. The effect of isostasy develops a non-negligible forces system that acts in combination with the collision process between the North China Craton and the South China Craton, which favors the growth of the Qinling orogen.

6.3. Geodynamics of the lower crust in MQL

The lower crust plays a crucial role in the continental evolution and mountains building (Liu and Gao, 1992), since it is directly related to the processes of material exchange between crust and mantle (Artemieva and Meissner, 2012). The physical properties of the lower crust in MQL are summarized as follows: (1) Low velocity (Teng et al., 2014a). The P-wave velocity ranges between 6.5 and 6.9 km/s and has an average value of 6.6 km/s (Teng et al., 2014a, 2014b), which is smaller than the average value of 7.14 km/s for the lower crust in continental domain (Rudnic and Fountain, 1995) and even than 6.8 km/s, which is its characteristic value in the DBTB area (Teng et al., 2014a, 2014b). (2) Low density of 2.8 g/cm^3 (this study). (3) Low Poisson ratio. According to recent results based on receiver functions (Si, 2015; Si et al., 2016), Poisson ratio is between 0.22 and 0.26 in MQL, which is obviously below the values 0.25–0.28 corresponding to other tectonic units along the B-B′ segment, and is also less than the mean value of 0.27 for the global continental crust (George and Charles, 1995); (4) Lower crust comparatively thinner in MQL than in DBTB, as much as 10 km, and a weak mountain root (Teng et al., 2014a, and this study).

The possible interpretation of this picture may be that the lower crust underwent a delamination beneath MQL, after which the crust lost the weight that could keep it isostatically stable above the upper mantle, which in turn resulted in its gradual elevation and decrease in seismic velocity, density and Poisson ratio. Although post-orogenic extension could also be the probable cause of the thin crust beneath MQL, it would be difficult to explain the properties of low velocity, low density and low Poisson ratio of the lower crust, since only simple extension cannot result in the compositional changes required by differences in velocities or densities (Gao et al., 1999).

Results provided by deep seismic reflection profiling suggest that DBTB is an accompanying product of the northward subduction of the South China Block, so that the crust is shortened and thickened in DBTB under a regional compression system (Dong et al., 2013). Meanwhile, the northern margin of the South China Block, which contains mafic intrusions, was probably dragged below MQL to the Paleo-Tethys subduction zone during the terminal closing stage of the ancient ocean, and was then surrounded by hot hydrated mantle materials, thus increasing the temperature and fluid content in the lower crust. This would have caused phase changes in the materials of the lower crust from granulite/gabbro to eclogite/garnet pyroxenite (Artemieva and Meissner, 2012; Austrheim et al., 1997; Bjomerud et al., 2002; Krystopowicz and Currie, 2013), and this "eclogization" would have increased the density of the lower crust by ~0.3 g/cm^3 (Bascoua et al., 2001), making it gravitationally unstable and susceptible to detach and sink in the mantle. Consequently, the change from mafic crust to eclogite might have facilitated the prolonged continental convergence during the Jurassic, causing not only the thrust in DBTB (Dong et al., 2013), but also the delamination of the lower crust below MQL.

Although strictly speaking the results obtained in this work do not provide direct evidence of the existence of delamination of the lower crust in MQL, whose strength would not be as great as in the East Qinling Orogen (He et al., 1998; Yuan et al., 1994; Zhang et al., 1996), the earlier features of low velocity, density and Poisson ratio contribute to support such delamination of the lower crust, whose current isostatic state implies that the Qinling Mountains may continue its growth due to the buoyancy effect.

7. Conclusions

This study presents the most recent gravity dataset collected along a 1000-km-long north-south profile that extends from Yuquan in the Sichuan Basin to Yulin in the Ordos Basin across the Middle Qinling Mountains and the Weihe Graben. The Bouguer gravity anomaly varies from −200 to −110 mGal along this profile. Based on high-quality gravity data and accredited velocity-density relationships, a density model was initially constructed to later obtain through interactive simulation the density model for the crust and uppermost mantle in the Middle Qinling Orogen and surrounding areas. This model reveals a rather low average density of 2.8 g/cm^3, but remarkable differences both in vertical direction (from 2.65 to 2.95 g/cm^3) and laterally, at the same time that shows clearly the crystalline basement, the Conrad interface separating the upper crust from the lower crust and the Moho discontinuity. The gravity field calculated by interactive modeling from the final density distribution model correlates well with the observed gravity field within a standard deviation of 1.26 mGal.

A combined isostatic compensation model that takes advantage of the Airy and Pratt's hypotheses has been used for the study of the isostatic equilibrium state of the crust without any loss of accuracy. A small discrepancy has been found between the isostatic Moho depth and the Moho depth previously obtained from gravity and density data, which leads us to suggest a future crust growth in Qinling in contrast with the Ordos and Sichuan basins that will remain stable.

Considering that more than 90% of the earthquakes occurred in the area have the hypocenter in the upper crust, the Conrad interface plays the role of a rheological transition zone separating the brittle crust from the ductile crust. The lack of seismicity between the Qinling Orogen and the Weihe Graben indicates increased stresses in the zone in response to the active collision between the South China Block and the North China Block.

Finally, considering the geophysical properties of the lower crust in Quinling, such as low seismic velocity, low density, low Poisson coefficient, fine crust and weak crustal root, it is concluded that the delamination of the lower crust is a feasible or reasonable interpretation.

Acknowledgements

The authors want to thank the aid of all people who have made this study possible, especially the observers and technicians who participated in the fieldwork. We are very grateful to Professor Walter D. Mooney, Dr. Guo Lianghui, Deng Yangfan and two anonymous reviewers for their comments and suggestions to improve the presentation of this paper. The China Earthquake Administration (CEA) provided the two gravimeters used in this research. The Ministry of Land and Resources of China (SinoProbe-03) and the National Natural Science Foundation of China (grants Nos. 41574082, 41204063, 90914012 and 41204096) funded this research.

References

Aitken, A.R.A., 2010. Moho geometry gravity inversion experiment (MoGGIE): a refined model of the Australian Moho, and its tectonic and isostatic implications. Earth Planet. Sci. Lett. 297, 71–83.
Ames, L., Zhou, G., Xiong, B., 1996. Geochronology and isotopic character of ultrahigh-pressure metamorphism with implications for collision of the Sino-Korean and Yangtze cratons, central China. Tectonics 15, 472–489.
Artemieva, I.M., Meissner, R., 2012. Crustal thickness controlled by plate tectonics: a review of crust-mantle interaction processes illustrated by European examples. Tectonophysics 530–531, 18–49.
Artemjev, M.E., Kaban, M.K., Kucherinenko, V.A., Demyanov, G.V., Taranov, V.A., 1994. Subcrustal density inhomogeneities of Northern Eurasia as derived from the gravity data and isostatic models of the lithosphere. Tectonophysics 240, 249–280.
Austrheim, H., Erambert, M., Engvik, A.K., 1997. Processing of crust in the root of the Caledonian continental collision zone: the role of eclogitization. Tectonophysics 273, 129–153.
Bascoua, J., Barruola, G., Vaucheza, A., Mainpricea, D., Egydio-Silva, M., 2001. EBSD-measured lattice-preferred orientations and seismic properties of eclogites. Tectonophysics 342, 61–80.
Bjomerud, M.G., Austrheim, H., Lund, M.G., 2002. Processes leading to eclogitization (densification) of subducted and tectonically buried crust. J. Geophys. Res. 107 (B10), 2252.
Burchfiel, B.C., Royden, L.H., van der Hilst, R.D., Hager, B.H., Chen, Z., King, R.W., Li, C., Lu, J., Yao, H., Kirby, E., 2008. A geological and geophysical context for the Wenchuan earthquake of 12 May 2008, Sichuan, People's Republic of China. GSA Today 18, 7.
Burov, E.V., Kogan, M.G., Lyon-Caen, H., Molnar, P., 1990. Gravity anomalies, the deep structure, and dynamic processes beneath the Tien Shan. Earth Planet. Sci. Lett. 96, 367–383.
Chen, W.P., Molnar, P., 1983. Focal depths of intracontinetal and itraplate earthquakes and their implications for the thermal and mechanical properties of the lithosphere. J. Geophys. Res. 88, 4183–4214.
Chen, W.P., 1988. A brief update on the focal depths of intracontinental earethquakes and their correllations with heat flow and tectonic age. Seismol. Res. Lett. 59, 263–272.
Cheng, S.Y., Zhang, G.W., Li, L., 2003. Lithospheric electrical structure of the Qinling orogen and its geodynamic implication. Chin. J. Geophys. 46 (3), 390–397.
Christensen, N.I., Mooney, W.D., 1995. Seismic velocity structure and composition of the continental crust: A global view. J. Geophys. Res. 100 (B7), 9761–9788.
Deng, Y., Zhang, Z., Badal, J., Fan, W., 2014. 3-D density structure under South China constrained by seismic velocity and gravity data. Tectonophysics 627, 159–170.
Dong, S.W., Gao, R., Yin, A., Guo, T.L., Zhang, Y.Q., Hu, J.M., Li, J.H., Shi, W., Li, Q.S., 2013. What drove continued continent-continent convergence after ocean closure? Insights from high-resolution seismic-reflection profiling across the Daba Shan in central China. Geology 41 (6), 671–674.
Dong, Y.P., Santosh, M., 2016. Tectonic architecture and multiple orogeny of the Qinling Orogenic Belt, Central China. Gondwana Res. 29 (1), 1–40.
Dong, Y.P., Zhang, G.W., Hauzenberger, C., Neubauer, F., Yang, Z., Liu, X.M., 2011a. Paleozoic tectonics and evolutionary history of the Qinling orogen: evidence from geochemistry and geochronology of ophiolite and related volcanic rocks. Lithos 122, 39–56.
Dong, Y.P., Zhang, G.W., Neubauer, F., Liu, X., Genser, J., Hauzenberger, C., 2011b. Tectonic evolution of the Qinling orogen, China: Review and synthesis. J. Asian Earth Sci. 41, 213–237.
Dong, Y.P., Zhang, G.W., Zhao, X., Yao, A.P., Liu, X.M., 2004. Geochemistry of the subduction-related magmatic rocks in the Dahong Mountains, northern Hubei Province: constraint on the existence and subduction of the eastern Mianlue oceanic basin. Sci. China (Ser. D) 47, 366–377.
Dong, Y.P., Liu, X.M., Zhang, G.W., Chen, Q., Zhang, X.N., Li, W., Yang, C., 2012. Triassic diorites and granitoids in the Foping area: Constraints on the conversion from subduction to collision in the Qinling orogen, China. J. Asian Earth Sci. 47, 123–142.
Dong, Y.P., Zhang, X.N., Liu, X.M., Li, W., Chen, Q., Zhang, G.W., Zhang, H.F., Yang, Z., Sun, S.S., Zhang, F.F., 2015. Propagation tectonics and multiple accretionary processes of the Qinling Orogen. J. Asian Earth Sci. 104, 84–98.
Faure, M., Lin, W., Le Breton, N., 2001. Where is the North China-South China block boundary in eastern China? Geology 29, 119–122.
Feng, R., Yan, H.F., Zhang, R.S., 1986. The rapid inversion of 3-D potential field and program design. Acta Geol. Sin. 60 (4), 390–403 (in Chinese).
Fu, G.Y., Gao, S.H., Freymueller, J.T., Zhang, G.Q., Zhu, Y.Q., Yang, G.L., 2014. Bouguer gravity anomaly and isostasy at western Sichuan Basin revealed by new gravity surveys. J. Geophys. Res. (Solid Earth) 119, 3924–3938.
Gao, R., Wang, H.Y., Zeng, L.S., Zhang, J.S., Guo, T.L., Li, Q.S., Li, W.H., Li, P., Guan, Y., 2014. The crust structures and the connection of the Songpan block and West Qinling orogen revealed by the Hezuo-Tangke deep seismic reflection profiling. Tectonophysics 634, 227–236.
Gao, S., Zhang, B.R., Gu, X.M., Xie, Q.L., Gao, C.L., Guo, X.M., 1995. Silurian-Devonian provenance changes of South Qinling basins: implications for accretion of the Yangtze (South China) to the North China Cratons. Tectonophysics 250, 183–197.
Gao, S., Zhang, B.R., Jin, Z.M., 1999. Lower crustal delamination in the Qinling-Dabie orogenic belt. Sci. China (Ser. D) 42 (4), 423–433.
George, Z., Charles, J.A., 1995. Continental crust composition constrained by measurements of crustal Poisson's ratio. Nature 374, 152–154.
Hacker, B.R., Ratschbacher, L., Webb, L., Ireland, T., Walker, D., Dong, S.W., 1998. U/Pb zircon ages constrain the architecture of the ultrahigh-pressure Qinling-Dabie Orogen, China. Earth Planet. Sci. Lett. 161, 215–230.
He, J.K., Liu, F.T., Liu, J.H., Sun, R.M., 1998. The morphology of Moho discontinuity and its evolution geodynamics in the eastern Qinling collisional orogenic belt. Chin. J. Geophys. 41 (S1), 64–76.
He, R.Z., Liu, G.C., Golos, E., Gao, R., Zheng, H.W., 2014. Isostatic gravity anomaly, lithospheric scale density structure of the northern Tibetan plateau and geodynamic causes for potassic lava eruption in Neogene. Tectonophysics 628, 218–227.
Hu, G.Z., Teng, J.W., Ruan, X.M., Yan, Y.F., Wang, P., Xiong, S.Q., 2014. Magnetic anomaly characteristics and crystalline basement variation of the Qinling orogenic belt and its adjacent areas. Chin. J. Geophys. 57 (2), 556–571 (in Chinese with abstract in English).
Hu, J.M., Che, H., Qu, H.J., Wu, G.L., Yang, J.X., Zhang, Z.Y., 2012. Mesozoic deformations of the Dabashan in the southern Qinling orogen, central China. J. Asian Earth Sci. 47, 171–184.
Huang, R., Zhu, L.P., Xu, Y.X., 2014. Crustal structure of Hube province of China from teleseismic receiver functions: Evidence for lower crust delamination. Tectonophysics 636, 286–292.
Jacoby, W., Smilde, L., 2009. Gravity Interpretation: Fundamentals and Application of Gravity Inversion and Geological Interpretation. Springer-Verlag, Berlin, Heidelberg, pp. 1–395.
Jia, S.X., Zhang, X.K., 2005. Crustal structure and comparison of different tectonic blocks in North China. Chin. J. Geophys. 48 (3), 611–620 (in Chinese with abstract in English).
Jordan, T.A., Watts, A.B., 2005. Gravity anomalies, flexure and the elastic thickness structure of the India-Eurasia collisional system. Earth Planet. Sci. Lett. 236, 732–750.
Krystopowicz, N.J., Currie, C.A., 2013. Crustal eclogitization and lithosphere delamination in orogens. Earth Planet. Sci. Lett. 361, 195–207.
Li, J.H., Dong, S.W., Yin, A., Zhang, Y.Q., Shi, W., 2015. Mesozoic tectonic evolution of the Daba Shan Thrust Belt in the southern Qinling orogen, central China: constraints from surface geology and reflection seismology. Tectonics 34, 1545–1575.
Li, J.H., Zhang, Y.Q., Dong, S.W., Shi, W., 2013. Structural and geochronological constraints on the Mesozoic tectonic evolution of the North Dabashan zone, South Qinling, central China. J. Asian Earth Sci. 64, 99–114.
Li, P.Y., Zhang, J.J., Guo, L., Yang, X.Y., 2012. Structural features and deformational ages of the northern Dabashan thrust belt. Geosci. Front. 3 (1), 41–49.
Li, S.G., Sun, W.D., Zhang, G.W., 1996. Chronology and geochemistry of metavolcanic rocks from Heigouxia valley in Mian-Lue tectonic belt, South Qinling: evidence for a Paleozoic oceanic basin and its close time. Sci. China (Ser. D) 39, 300–310.
Li, S.Z., Kusky, T.M., Wang, L., Zhang, G.W., Lai, S.C., Liu, X.C., Dong, S.W., Zhao, G.C., 2007. Collision leading to multiple-stage large-scale extrusion in the Qinling orogen: insights from the Mianlue suture. Gondwana Res. 12, 121–143.
Liu, C.Y., Zhao, H.G., Gui, X.J., Yue, L.P., Zhao, J.F., Wang, J.Q., 2006. Space-time coordinates of the evolution and reformation and mineralization response in Ordos basin. Acta Geol. Sin. 80 (5), 617–638 (in Chinese with abstract in English).
Liu, Q.S., Gao, S., 1992. Geophysical properties of the lower crustal granulite from the Qinling orogenic belt, China. Tectonophysics 204 (3–4), 401–408.
Ludwig, W.J., Nafe, J.E., Drake, C.L., 1970. Seismic refraction. The Sea 4, 53–84.
Lyon-Gaen, H., Molnar, P., 1984. Gravity anomalies and the structure of western Tieta and the southern Tarim basin. Geophys. Res. Lett. 11, 1251–1254.
Maggi, A., Jackson, J.A., McKenzie, D., Priestley, K., 2000. Earthquake focal depths, effective elastic thickness, and the strength of the continental lithosphere. Geology 28 (6), 495–498.
Mattauer, M., Matte, Ph., Malavieille, J., Tapponnier, P., Maluski, H., Xu, Z., Lu, Y., Tang, Y., 1985. Tectonics of the Qinling Belt: build-up and evolution of eastern Asia. Nature 317, 496–500.
Meng, Q.R., Zhang, G.W., 1999. Timing of collision of the North and South China blocks: controversy and reconciliation. Geology 27, 123–126.
Meng, Q.R., Zhang, G.W., 2000. Geologic framework and tectonic evolution of the Qinling orogen, central China. Tectonophysics 323, 183–196.
Mooney, W.D., Braile, L.W., 1989. The seismic structure of the continental crust and upper mantle of North America. In: Bally, A.W., Palmer, A.R. (Eds.), The Geology of North America, An Overview. In Geological Society of America, Boulder, Colorado, pp. 39–52.

Mooney, W.D., Vidale, J.E., 2003. Thermal and chemical variations in subcrustal cratonic lithosphere: evidence from crustal isostasy. Lithos 71, 185–193.
Moritz, H., 1980. Geodetic reference system 1980. Bull. Géodés. 54, 395–405.
Nafe, J.E., Drake, C.L., 1957. Variation with depth in shallow and deep water marine sediments of porosity, density and the velocities of compressional and shear waves. Geophysics 22 (3), 523–552.
Peltzer, G., Tapponnier, P., 1988. Formation and evolution of strike-slip faults, rifts, and basins during the India-Asia collision: an experimental approach. J. Geophys. Res. (Solid Earth) 93, 15085–15117.
Peng, J.B., Zhang, J., Su, S.R., 1992. Active Fault and Geological Disaster of Weihe Basin. Northwest University Press (in Chinese), Xi'An.
Ratschbacher, L., hacker, B.R., Calvert, A., Webb, L.E., Grimmer, J.C., McWilliams, M.O., Ireland, T., Dong, S., Hu, J., 2003. Tectonics of the Qinling (Central China): tectonostratigraphy, geochronology, and deformation history. Tectonophysics 366, 1–53.
Ratschbacher, L., Franz, L., Enkelmann, E., Jonckeere, R., Poerschke, A., Hacker, B.R., Dong, S.W., Zhang, Y.Q., 2006. The Sino-Korean-Yangtze suture, the Huwan detachment, and the Paleozoic-Tertiary exhumation of (ultra) high-pressure rocks along the Tongbai-Xinxian-Dabie Mountains. Geol. Soc. Am., Spec. Publ. 403, 45–75.
Ren, J., Peng, J.B., Wang, F.Y., Liu, C., Feng, X.J., Dai, W.Q., 2012. The research of deep structural features of Weihe basin and adjacent areas. Chin. J. Geophys. 55 (9), 2939–2947 (in Chinese with abstract in English).
Rudnic, R.L., Fountain, D.M., 1995. Nature and composition of the continental crust: A lower crustal perspective. Rev. Geophys. 33 (3), 267–309.
Segev, A., Rybakov, M., Lyakhovsky, V., Hofstetter, A., Tibor, G., Goldschmidt, V., Avraham, Z.B., 2006. The structure, isostasy and gravity field of the Levant continental margin and the southeast Mediterranean area. Tectonophysics 425, 137–157.
Sengor, A.M.C., 1985. East Asia Tectonic Collage. Nature 318, 16–17.
Shi, W., Li, J.H., Tian, M., Wu, G.L., 2013. Tectonic evolution of the Dabashan orocline, central China: insights from the superposed folds in the eastern Dabashan foreland. Geosci. Front. 4 (6), 729–741.
Shi, W., Zhang, Y.Q., Dong, S.W., Hu, J.M., Wiesinger, M., Ratschbacher, L., Jonckheere, R., Li, J.H., Tian, M., Chen, H., Wu, G.L., Ma, L.C., Li, H.L., 2012. Intra-continental Dabashan orocline, southwestern Qinling, Central China. J. Asian Earth Sci. 46 (2), 20–38.
Si, X., 2015. The velocity structures and dynamics in crust and upper mantle of the Qinling orogenic belt and the region on its north and south margins from teleseismic receiver function. Ph.D. thesis. Institute of Geology and Geophysics, Chinese Academy of Sciences (in Chinese with abstract in English).
Si, X., Teng, J.W., Liu, Y.S., Ma, X.Y., Qiao, Y.H., Dong, X.P., Song, P.H., 2016. Crust and upper mantle velocity structure of the Qinling orogenic and the region on its north and south margins from teleseismic receiver function. Chin. J. Geophys. 59 (4), 1321–1334 (in Chinese with abstract in English).
Teng, J.W., Li, S.L., Zhang, Y.Q., Wang, F.Y., Pi, J.L., Zhao, J.R., Zhang, C.K., Qiao, Y.H., Hu, G.Z., Yan, Y.F., 2014a. Fine velocity structures and deep processes in crust and mantle of the Qinling orogenic belt and the adjacent North China craton and Yangtze craton. Chin. J. Geophys. 57 (10), 3154–3175 (in Chinese with abstract in English).
Teng, J.W., Li, S.L., Zhang, Y.Q., Zhao, J.R., Pi, J.L., Wang, F.Y., Yan, Y.F., Yang, H., Hu, G.Z., Pan, S.Z., 2014b. Seismic wave fields and dynamical response for Qinling orogen and sedimentary basins and crystalline basement. Chin. J. Geophys. 57 (3), 770–788 (in Chinese with abstract in English).
Tiwari, V.M., Vyghreswara Rao, M.B.S., Mishra, D.C., Singh, B., 2006. Crustal structure across Sikkim, NE Himalaya from new gravity and magnetic data. Earth Planet. Sci. Lett. 247, 61–69.
Turcotte, D.L., Schubert, G., 2002. Geodynamics, second ed. Cambridge University Press, London.
Ussami, N., Cogo de Sa, N., Molina, E.C., 1993. Gravity map of Brazil, regional and residual isostatic anomalies and their correlation with major tectonic provinces. J. Geophys. Res. 98, 2199–2208.
Wang, H.Y., Gao, R., Ma, Y.S., Zhu, X., Li, Q.S., Kuang, Z.Y., Li, P., Lu, Z.W., 2007. Basin-range coupling and lithosphere structure between the Zoige and the west Qinling. Chin. J. Geophys. 50 (2), 472–481 (in Chinese with abstract in English).
Wang, J.W., Li, R.H., Hu, K.Y., Zhang, J.S., Liao, S.Z., 2010. Basic physical features of regional rocks in Anhui province. Geol. Anhui. 20 (2), 112–116 (in Chinese with abstract in English).
Wang, P., Huang, Z.C., Mi, N., Xu, M.J., Wang, L.S., Li, H., Yu, D.Y., Huang, H., Mao, X.L., 2014. Crustal structure beneath the Weihe Graben in central China: evidence for the tectonic regime transformation in the Cenozoic. J. Asian Earth Sci. 81, 105–114.
Wang, Q.S., Teng, J.W., Zhang, Y.Q., Wen, W., Hua, C.C., 2013. Discussion on the special gravity field across the north part of Middle Qinling Mt. Chin. J. Geophys. 56 (3), 792–798 (in Chinese with abstract in English).
Watts, A.B., Burov, E.B., 2003. Lithospheric strength and its relationship to the elastic and seismogenic layer thickness. Earth Planet. Sci. Lett. 213, 113–131.
Wu, G.L., Meng, Q.R., Duan, L., Li, L., 2014. Early Mesozoic structural evolution of the eastern West Qinling, northwest China. Tectonophysics 630, 9–20.
Yang, J.J., 2002. Tectonic Evolution and Oil-Gas Reservoirs Distribution in Ordos Basin. Petroleum Industry Press, Beijing, pp. 1–85 (in Chinese with abstract in English).
Yuan, X.C., Xu, M.C., Tang, W.B., Wang, Q.H., 1994. Eastern Qinling seismic reflection profiling. Acta Geophys. Sinica 37 (6), 749–758 (in Chinese with abstract in English).
Zhang, C., Meng, Q.R., Yu, Z., Zhang, G.W., 1997. Geochemical characteristics and tectonic implication of gravels in the Hubaohe Conglomerate in the East Qinling. Acta Sedimentol. Sinica 15, 115–119 (in Chinese with abstract in English).
Zhang, G.W., Meng, Q.R., Lai, S.C., 1995. Tectonics and structure of the Qinling Orogenic belt. Sci. China (Ser. B) 38, 1379–1394.
Zhang, G.W., Meng, Q.R., Yu, Z., Sun, Y., Zhou, D., Guo, A., 1996. Orogenesis and dynamics of the Qinling Orogen. Sci. China (Ser. D) 39 (3), 225–234.
Zhang, G.W., Zhang, B.R., Yuan, X.C., 2001. Qinling Orogenic Belt and Continental Dynamics. Science Press, Beijing (in Chinese).
Zhang, J.S., Gao, R., Li, Q.S., Wang, H.Y., Zhu, H., 2007. A study on geophysical characteristic and basement in the Songpan-Garze and Western Qinling Orogenic Belt. Geol. Rev. 53 (2), 261–267 (in Chinese with abstract in English).
Zhang, J.S., Gao, R., Zeng, L.S., Li, Q.S., Guan, Y., He, R.Z., Wang, H.Y., Lu, Z., 2010a. Relationship between characteristics of gravity and magnetic anomalies and the earthquakes in the Longmenshan range and adjacent areas. Tectonophysics 491, 218–229.
Zhang, K., 1989. Tectonics and Resources of Ordos Fault Block. The Science and Technology Press of Shaanxi, Xi'an, pp. 1–81 (in Chinese).
Zhang, X.K., Jia, S.X., Zhao, J.R., Zhang, C.K., Yang, J., Wang, F.Y., Zhang, J.S., Liu, B.F., Sun, G.W., Pan, S.Z., 2008a. Crustal structures beneath West Qinling-East Kunlun orogen and its adjacent area- Results of wide-angle seismic reflection and refraction experiment. Chin. J. Geophys. 51 (2), 439–450 (in Chinese with abstract in English).
Zhang, Y.Q., Shi, W., Li, J.H., Wang, R.R., Li, H.L., Dong, S.W., 2010b. Formation mechanism of the Dabashan foreland arc-shaped structural belt. Acta Geol. Sin. 84 (9), 1300–1315 (in Chinese with abstract in English).
Zhang, Y.Q., 2013. The crustal structure beneath the Ordos basin and the orogens on its north and south margins. Post-Doc Research Report, Institute of Geology and Geophysics, Chinese Academy of Sciences (in Chinese with abstract in English).
Zhang, Y.Q., Mercier, J.L., Vergely, P., 1998. Extension in the graben systems around the Ordos (China), and its contribution to the extrusion tectonics of south China with respect to Gobi-Mongolia. Tectonophysics 285, 41–75.
Zhang, Y.Q., Teng, J.W., Wang, Q.S., 2010c. The crustal isostatic anomaly beneath eastern Tibet and western Sichuan and its relationship with the distribution of earthquakes. Chin. J. Geophys. 53 (11), 2631–2638 (in Chinese with abstract in English).
Zhang, Y.Q., Teng, J.W., Wang, Q.S., Hu, G.Z., 2014. Density structure and isostatic state of the crust in the Longmenshan and adjacent areas. Tectonophysics 619–620, 51–57.
Zhang, Z.J., Zhang, X., Badal, J., 2008b. Composition of the crust beneath southeastern China derived from an integrated geophysical data set. J. Geophys. Res. 113, B04417.
Zhao, B., Bai, Z., Xu, T., Zhang, Z., Badal, J., 2013. Lithological model of the South China crust based on integrated geophysical data. J. Geophys. Eng. 10 (2). http://dx.doi.org/10.1088/1742-2132/10/2/025005.
Zheng, H.W., He, R.Z., Guo, X., 2009. Characteristics of the crustal and mantle structures across Lhasa terrane. Earthq. Sci. 22, 431–434.